






# Two-tier manipulation of holographic information

LIBIN YAN,<sup>1,2</sup> JIANLING XIAO,<sup>1,2</sup>  TOMASZ PLASKOCINSKI,<sup>1</sup>  
MOHAMMAD BIABANIFARD,<sup>1</sup>  SAYDULLA PERSHEYEV,<sup>1</sup> MEISAM  
ASKARI,<sup>1</sup> AND ANDREA DI FALCO<sup>1,\*</sup> 

<sup>1</sup>*SUPA, School of Physics and Astronomy, University of St Andrews, North Haugh, St Andrews, KY16 9SS, Scotland, UK*

<sup>2</sup>*These authors contributed equally to the paper*

\**adf10@st-andrews.ac.uk*

**Abstract:** Here we demonstrate the two-tier manipulation of holographic information using frequency-selective metasurfaces. Our results show that these devices can diffract light efficiently at designed frequency and environmental conditions. By changing the frequency and refractive index of the surrounding environment, the metasurfaces produce two different holographic images. We anticipate that these environmental dependent, frequency-selective metasurfaces will have practical applications in holographic encryption and sensing.

© 2022 Optica Publishing Group under the terms of the [Optica Open Access Publishing Agreement](#)

## 1. Introduction

Photonic metasurfaces with tailored sub-wavelength elements offer bespoke control of the polarization, phase and amplitude of the scattered electromagnetic wave, which enable a wide range of intriguing applications such as flat lenses [1,2], wave-plates [3] beam deflectors [4,5] and holograms [6]. Specifically, holographic metasurfaces have attracted great attention for applications in encryption [7,8], optical display [9–11] and sensing [12,13]. One of the key advantages of using metasurfaces as holographic plates is the possibility to encode the information into multiple physical properties of light, including orbital angular momentum [14,15], wavelength [16–18], polarization [19–22], and direction of propagation of the light [23,24]. Access to the holographic information can also be regulated dynamically by external actuations, such as chemical reaction [25,26], mechanical modifications [27–29] and change in the optical and physical properties of the surrounding medium [30,31]. In this work, we demonstrate holographic metasurfaces that reveal the encoded information when both light properties and external control parameters are suitably selected, thus implementing a reversible and tunable two-tier manipulation of the holographic information. The working principle of these metasurfaces is shown in Fig. 1, where different holographic images are obtained for specific wavelengths, in presence or absence of water on the metasurface. In Fig. 1(b), the conditions of wavelength  $\lambda_1$  (depicted in the red key) and surrounding medium  $M_1$  (depicted in the yellow key) are satisfied to grant access to a holographic image of the butterfly. With another set of “keys”, medium  $M_2$  and wavelength  $\lambda_2$ , one can gain access to the holographic image of a caterpillar, as shown in Fig. 1(c). The holographic images two-tier manipulated by the metasurface are non-correlated, independent, and can be arbitrary. This class of metasurfaces has promising applications in optical encryption and optical sensing. In the following, we first describe the design and fabrication of the metasurfaces, and the characterization setup. We then present and discuss the results, before concluding the paper.

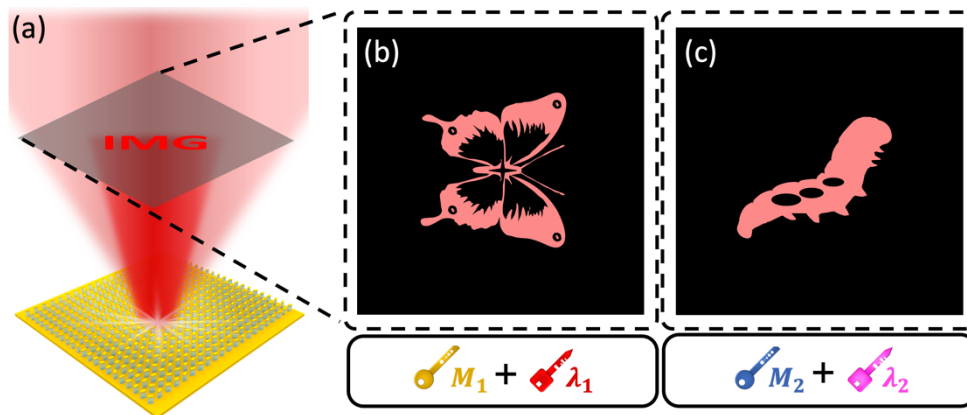


**Fig. 1.** (a) Schematic of metasurface with two-tier manipulation of holographic information. (b) Holographic image of a butterfly, accessed under the conditions of medium  $M_1$  and wavelength  $\lambda_1$ . (c) Holographic image of a caterpillar, accessed under the conditions of medium  $M_2$  and wavelength  $\lambda_2$ .

## 2. Methods

### 2.1. Design

In our work, the metasurfaces are designed to work in reflection. The targeted images are encoded using the Gerchberg-Saxton algorithm [32], with full Rayleigh-Sommerfeld integral as propagator [33]. The metasurface consists of two sets of subcells (meta-atoms), as shown in Figs. 2(a) and 2(b), with a resolution of  $400 \times 400$  pixels and pixel size of 500 nm. The subcells geometry is derived from the popular three layers approach, typically used to create reflective-type metallic metasurfaces with Pancharatnam-Berry (PB) phase elements [34]. In the traditional design, a metallic nano-rod is separated by a dielectric spacer from a reflective background plane and its orientation on the plane is directly linked to the phase of the reflected cross circularly polarized light. In our design, the dielectric layer underneath the nanorods is not uniform, and the meta-atoms are composed of polymeric pillars capped with a thin 40 nm metallic layer, standing upright on a fully reflective background plane mirror. A structured dielectric layer mediates the frequency selective behavior of the meta-atoms and increases the dependency from the refractive index of the surrounding medium. For subcell-1, the length  $L_1$  and width  $W_1$  of the pillars are 245 nm and 143 nm, respectively. For subcell-2, the length  $L_2$  and width  $W_2$  of the pillars are 185 nm and 115 nm, respectively. For both designs, the unit period  $P$  is 500 nm, the height of the pillar  $T_p$  is 310 nm, and the thin metallic layer  $T$  is 40 nm. The model also includes the presence of a 5 nm thin interstitial layer of polymer between the background metallic layer and the additional metallic cap, which results from the constraints of the experimental fabrication method (see the fabrication section below). The electromagnetic response of the meta-atoms was studied using the software Computer Simulation Technology (CST). Figures 2(c) and 2(d) show the calculated reflectivity versus wavelength in the dry and wet conditions for both subcells, for circular polarization. Fig. S1 shows the reflectivity of the subcells for different orientations of the pillars and the calculated dephasing induced.

Figure 2(e) shows the contrast of the reflectivity between the two subcell designs. The results show that subcell-1 has a substantially higher reflectivity than subcell-2 when the sample is dry at a wavelength of 705 nm, whereas in wet conditions subcell-2 is more reflective than subcell-1 for a wavelength of 735 nm. Importantly, at these two wavelengths, the efficiency of the low reflecting subcell is low enough to allow only one image to be displayed.

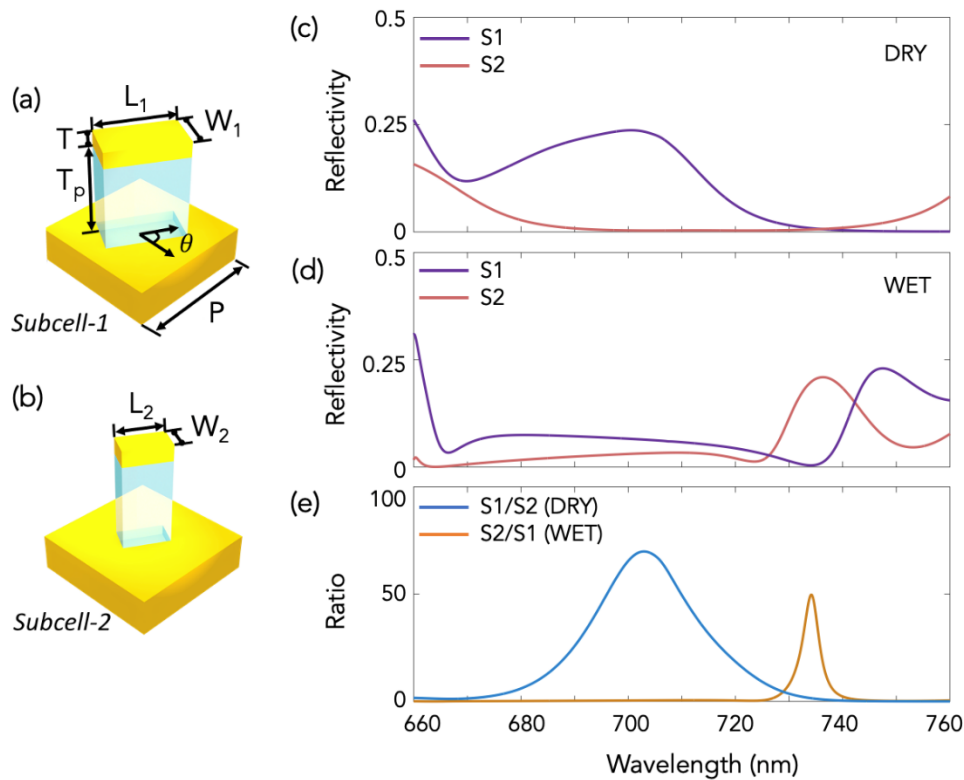


**Fig. 2.** Schematic of (a) Subcell-1 and (b) Subcell-2 for the metasurface. (c-d) Reflectivity of Subcell-1 and Subcell-2 for wavelength in the medium of air and water, respectively. (e) Ratio of reflectivity between holograms of Subcell-1 and Subcell-2 in air and between those of Subcell-2 and Subcell-1 in water.

The choice of the specific geometrical parameters was the outcome of an extensive numerical campaign, which used as boundary conditions the fabrication constraints. Importantly, the design of the two subcells aimed at increasing the ratio of their reflectivity at different wavelengths, for different environmental conditions, rather than their individual efficiencies. In Fig. S2 we show how the geometrical parameters of the subcells affect their respective reflectivity in both dry and wet conditions. We note that the reflectivity of two subcells is determined by the frequency of the supported resonant modes, which for subcell-1 and subcell-2 have a different dependence from the refractive index of the surrounding environment. Fig. S3 shows the field distribution of the key modes that determine the optical response of the meta-atoms and their dependence on the main geometrical parameters.

## 2.2. Fabrication

Figure 3(a) shows the fabrication process. The substrate was a silicon die, which was initially cleaned in ultrasonic bath in acetone and isopropanol, for 10 minutes each. We then deposited with an electron beam evaporator (Edward AUTO306) an adhesions layer of 5 nm NiCr followed by a 150 nm thick gold layer as background plane. We then spin coated a 310 nm-thick layer of the e-beam resist Ma-N 2403 (Micro Resist Technology) at 3000 rpm for 60 s and baked the sample for 15 minutes at 90°C. The holographic pattern was defined using a Raith eLINE Plus Electron Beam Lithography (EBL) system, with a dose of 250  $\mu\text{C}/\text{cm}^2$ , followed by 10 minutes of post-exposure baking at 90 °C and development using Ma-D (Micro Resist Technology) for

100 s, followed by an isopropanol wash. Finally, a 40 nm thick gold cap was evaporated on the developed sample. This process produces a small step on the gold layer at the base of the pillars, which was included in the numerical model of the meta-atoms. This procedure has the practical advantage of not requiring lift-off or etch-back approaches to realize the meta-atoms. However, after the development of the exposed pillars, we consistently observed a thin residual layer of polymer in the patterned area. This is due to the limited acceleration voltage of our e-beam system and the fact that the pillars are defined on a gold background. This interstitial layer was also included in the modelling, with a thickness of 5 nm, consistently with the experimental observation. Figures 3(b) and 3(c) are two Scanning Electron Microscope (SEM) images of the fabricated samples for dry and wet designs, where the scale bar is 500 nm.

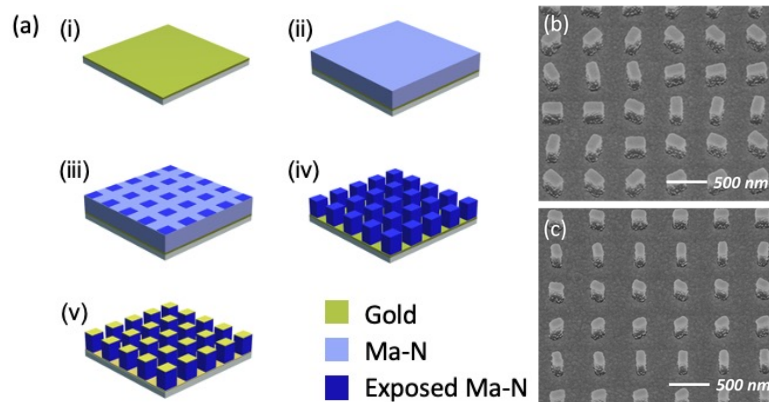


**Fig. 3.** (a) Fabrication processes of the metasurface. SEM image of (b) Subcell-1 and (c) Subcell-2.

### 2.3. Experimental measurement

To measure the efficiency and viability of the metasurfaces we designed two holograms producing a collimated spot of 1 mm in diameter at an angle of 30 degrees, respect to the normal. Each metasurface was  $100 \times 100 \mu\text{m}^2$  wide, tiled in  $2 \times 2$  configuration, to minimize the effect of speckling on the quality of the image, as customary [35]. A broadband laser (SuperK NKT photonics) was circularly polarized, expanded to a beam with diameter of 1.5 cm with a telescope made by two lenses with focal length 50 mm and 400 mm and then focused on the metasurface with a lens with focal distance 750 mm. The setup produced a spot size of  $\sim 250 \mu\text{m}$  diameter at the metasurface. The collimated spot generated by the holograms was collected with a silicon power meter (Thorlabs PM200), while sweeping the wavelength of the incident light using the SuperK SELECT module, which extracts from the supercontinuum source pulses with bandwidth in the  $\sim 1\text{-}3 \text{ nm}$  range.

The experiment was repeated for subcell-1 and subcell-2 in both wet and dry conditions. For the wet experiment, the sample was placed in a petri dish, filled with enough water to create a flat interface, to avoid introducing aberration artefacts due to potential water menisci. In this configuration, the free surface of the water was at about 2 mm from the metasurface. This distance was sufficient to prevent issues related to multiple interference of light at the two interfaces. The holograms were designed to produce an image on reflection at an angle of 30 degrees with respect to the normal to the surface, thus much smaller than the total internal reflection angle at the water/air interface. The ratios of the reflected power collected in the spot for the two types of meta-atoms, both in dry and wet environments are shown in Fig. 4(a). The efficiency of the

holograms in dry and wet conditions are shown in Fig. S4. The efficiency was corrected by the spot size to metasurface area ratio.

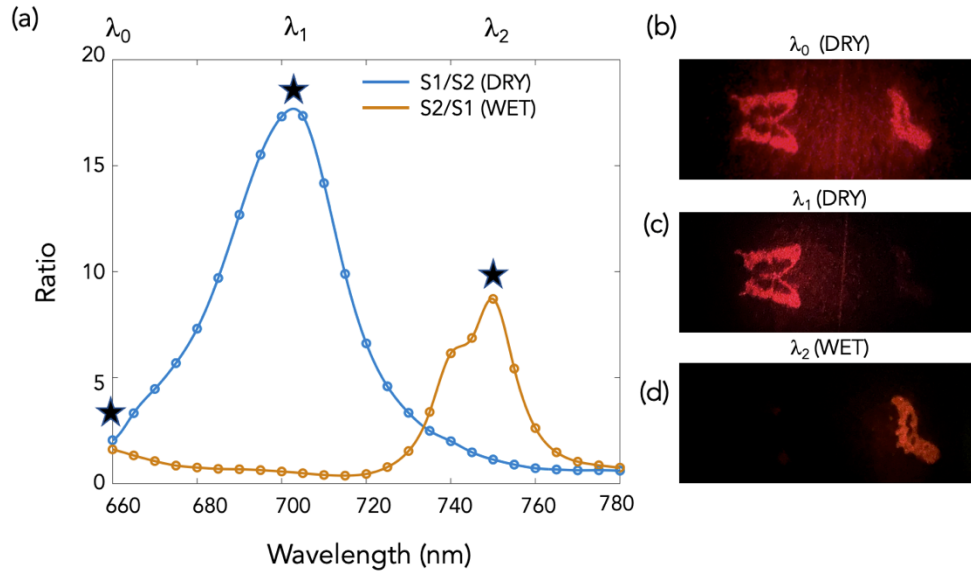


**Fig. 4.** Experimental measurements of the holographic metasurfaces under different conditions. (a) Solid blue and orange lines demonstrate the relative efficiency of the subcell-1 to subcell-2 in dry and wet conditions. (b) Holographic pattern generated using 660 nm wavelength in dry condition. (c) Holographic pattern generated using 705 nm wavelength in dry condition. (d) Holographic pattern generated using 750 nm wavelength in wet conditions.

The second pattern was a  $2 \times 2$  checkerboard pattern with 200  $\mu\text{m}$  metasurfaces of subcell-1 and subcell-2 fabricated side by side. The subcell-1 metasurfaces produced a butterfly image in the imaging plane, whereas subcell-2 produced a caterpillar image in the imaging plane. The holographic metasurfaces were designed to produce images with side of 2 cm, for an imaging plane oriented at 30 degrees with respect to the normal, 10 cm away from the metasurface. The incoming laser beam spot was slightly defocused to cover the whole pattern, which was characterized at different wavelengths and environmental conditions, as shown in Figs. 4(b)-(d).

### 3. Discussion and conclusions

The results of Fig. 4(a) clearly confirm that the metasurface pattern produces two distinct images when the designed wavelength is selected, and the environmental conditions are satisfied. The ratios of the hologram efficiencies were obtained measuring the reflectivity spectra for dry and wet samples. The experimental ratios had maximum values for  $\lambda_1 = 705$  nm (dry condition) and  $\lambda_2 = 750$  nm (wet condition). We attribute the shift of the peak of the ratio of the efficiencies in the wet case to partial wetting and fabrication imperfections, which affect more strongly the modes with high intensity at the sharp corners of the capping and background layers, responsible for the wet operation (see again Fig. S3 and Fig. S4).

The holographic images shown in panels (b)-(d) of Fig. 4 were projected on a thin diffusive screen and acquired with a camera with the same exposure parameters, for the same laser power. The results clearly demonstrate that the metasurfaces can implement the two-tier encoding scheme, showing different images with very good contrast at different wavelengths, for different environmental conditions.



In conclusion, we have presented a holographic metasurface for two-tier manipulation of the holographic information. The two-tier manipulation is realized by combining the intrinsic physical property of the light with external control factors. In our design, the reflective response of the metasurface is tailored using both surrounding medium and incident wavelength. For a specific combination of medium and wavelength, the metasurface produces a determined holographic image. When both a different medium and wavelength are selected, the metasurface produces a different holographic image. Such a holographic metasurface paves the way for multi-degree-of-freedom manipulations of holographic information, which has promising applications in holographic information encryption and sensing.

**Funding.** European Research Council under the Horizon 2020 Framework Programme Research and Innovation Program (819346).

**Disclosures.** The authors declare that they have no conflict of interest.

**Data availability.** Data underlying the results presented in this paper are available in Ref. [36].

**Supplemental document.** See [Supplement 1](#) for supporting content.

## References

1. N. Yu and F. Capasso, "Flat optics with designer metasurfaces," *Nat. Mater.* **13**(2), 139–150 (2014).
2. M. Khorasaninejad, A. Y. Zhu, C. Roques-Carnes, W. T. Chen, J. Oh, I. Mishra, R. C. Devlin, and F. Capasso, "Polarization-Insensitive Metalenses at Visible Wavelengths," *Nano Lett.* **16**(11), 7229–7234 (2016).
3. D.-Q. Zhang, F.-Z. Shu, Z.-W. Jiao, and H.-W. Wu, "Tunable wave plates based on phase-change metasurfaces," *Opt. Express* **29**(5), 7494–7503 (2021).
4. N. Li, Y. H. Fu, Y. Dong, T. Hu, Z. Xu, Q. Zhong, D. Li, K. H. Lai, S. Zhu, and Q. Lin, "Large-area pixelated metasurface beam deflector on a 12-inch glass wafer for random point generation," *Nanophotonics* **8**(10), 1855–1861 (2019).
5. S. Sun, K.-Y. Yang, C.-M. Wang, T.-K. Juan, W. T. Chen, C. Y. Liao, Q. He, S. Xiao, W.-T. Kung, and G.-Y. Guo, "High-efficiency broadband anomalous reflection by gradient meta-surfaces," *Nano Lett.* **12**(12), 6223–6229 (2012).
6. Q. Jiang, G. Jin, and L. Cao, "When metasurface meets hologram: principle and advances," *Adv. Opt. Photonics* **11**(3), 518 (2019).
7. G. Qu, W. Yang, Q. Song, Y. Liu, C.-W. Qiu, J. Han, D.-P. Tsai, and S. Xiao, "Reprogrammable meta-hologram for optical encryption," *Nat. Commun.* **11**(1), 1–5 (2020).
8. H. Rajabalipanah, K. Rouhi, A. Abdolali, S. Iqbal, L. Zhang, and S. Liu, "Real-time terahertz meta-cryptography using polarization-multiplexed graphene-based computer-generated holograms," *Nanophotonics* **9**(9), 2861–2877 (2020).
9. I. Kim, G. Yoon, J. Jang, P. Genevet, K. T. Nam, and J. Rho, "Outfitting next generation displays with optical metasurfaces," *ACS Photonics* **5**(10), 3876–3895 (2018).
10. G.-Y. Lee, J.-Y. Hong, S. Hwang, S. Moon, H. Kang, S. Jeon, H. Kim, J.-H. Jeong, and B. Lee, "Metasurface eyepiece for augmented reality," *Nat. Commun.* **9**(1), 1–10 (2018).
11. T. Hu, C.-K. Tseng, Y. H. Fu, Z. Xu, Y. Dong, S. Wang, K. H. Lai, V. Bliznetsov, S. Zhu, and Q. Lin, "Demonstration of color display metasurfaces via immersion lithography on a 12-inch silicon wafer," *Opt. Express* **26**(15), 19548–19554 (2018).
12. Y. Lee, S.-J. Kim, H. Park, and B. Lee, "Metamaterials and metasurfaces for sensor applications," *Sensors* **17**(8), 1726 (2017).
13. Y. Wang, C. Zhao, J. Wang, X. Luo, L. Xie, S. Zhan, J. Kim, X. Wang, X. Liu, and Y. Ying, "Wearable plasmonic-metasurface sensor for noninvasive and universal molecular fingerprint detection on biointerfaces," *Sci. Adv.* **7**(4), eabe4553 (2021).
14. H. Oraizi and H. Emamian, "Generation of orbital angular momentum modes via holographic leaky-wave metasurfaces," *Sci. Rep.* **10**(1), 7358 (2020).
15. R. C. Devlin, A. Ambrosio, D. Wintz, S. L. Oscurato, and F. Capasso, "Spin-to-orbital angular momentum conversion in dielectric metasurfaces," *Opt. Express* **25**(1), 377 (2017).
16. L. Huang, S. Zhang, and T. Zentgraf, "Metasurface holography: from fundamentals to applications," *Nanophotonics* **7**(6), 1169–1190 (2018).
17. E. Arbabi, A. Arbabi, S. M. Kamali, Y. Horie, and A. Faraon, "Multiwavelength metasurfaces through spatial multiplexing," *Sci. Rep.* **6**(1), 32803 (2016).
18. W. Ye, F. Zeuner, X. Li, B. Reineke, S. He, C.-W. Qiu, J. Liu, Y. Wang, S. Zhang, and T. Zentgraf, "Spin and wavelength multiplexed nonlinear metasurface holography," *Nat. Commun.* **7**(1), 11930 (2016).
19. T. Ze, X. Chen, H. Jiang, C. Zhang, and S. Liu, "Polarization multiplexed all-dielectric metasurfaces for wavefront manipulation in a transmission mode," *J. Opt.* **19**(10), 105102 (2017).
20. D. Wen, F. Yue, G. Li, G. Zheng, K. Chan, S. Chen, M. Chen, K. F. Li, P. W. H. Wong, and K. W. Cheah, "Helicity multiplexed broadband metasurface holograms," *Nat. Commun.* **6**(1), 8241 (2015).

21. W. T. Chen, K.-Y. Yang, C.-M. Wang, Y.-W. Huang, G. Sun, I.-D. Chiang, C. Y. Liao, W.-L. Hsu, H. T. Lin, and S. Sun, "High-efficiency broadband meta-hologram with polarization-controlled dual images," *Nano Lett.* **14**(1), 225–230 (2014).
22. J. P. Balthasar Mueller, N. A. Rubin, R. C. Devlin, B. Groever, and F. Capasso, "Metasurface Polarization Optics: Independent Phase Control of Arbitrary Orthogonal States of Polarization," *Phys. Rev. Lett.* **118**(11), 113901 (2017).
23. S. M. Kamali, E. Arbabi, A. Arbabi, Y. Horie, M. Faraji-Dana, and A. Faraon, "Angle-multiplexed metasurfaces: encoding independent wavefronts in a single metasurface under different illumination angles," *Phys. Rev. X* **7**(4), 041056 (2017).
24. A. Leitis, A. Tittl, M. Liu, B. H. Lee, M. B. Gu, Y. S. Kivshar, and H. Altug, "Angle-multiplexed all-dielectric metasurfaces for broadband molecular fingerprint retrieval," *Sci. Adv.* **5**(5), eaaw2871 (2019).
25. S. Saha, D. Shah, V. M. Shalaev, and A. Boltasseva, "Tunable Metasurfaces: Controlling Light in Space and Time," *Optics and Photonics News* **32**, 34–41 (2021).
26. Z. Li, X. Tian, C.-W. Qiu, and J. S. Ho, "Metasurfaces for bioelectronics and healthcare," *Nat. Electron.* **4**(6), 382–391 (2021).
27. J. Hu, S. Bandyopadhyay, Y.-H. Liu, and L.-Y. Shao, "A Review on Metasurface: From Principle to Smart Metadevices," *Front. Phys.* **8**, 502 (2021).
28. O. Quevedo-Teruel, H. Chen, A. Díaz-Rubio, G. Gok, A. Grbic, G. Minatti, E. Martini, S. Maci, G. V. Eleftheriades, and M. Chen, "Roadmap on metasurfaces," *J. Opt.* **21**(7), 073002 (2019).
29. S. M. Kamali, E. Arbabi, A. Arbabi, Y. Horie, and A. Faraon, "Highly tunable elastic dielectric metasurface lenses," *Laser Photonics Rev.* **10**(6), 1002–1008 (2016).
30. H. Cai, J. A. Dolan, G. S. Gordon, T. Chung, and D. López, "Polarization-insensitive medium-switchable holographic metasurfaces," *ACS photonics* **8**(9), 2581–2589 (2021).
31. B. Xiong, Y. Xu, J. Wang, L. Li, L. Deng, F. Cheng, R. W. Peng, M. Wang, and Y. Liu, "Realizing Colorful Holographic Mimicry by Metasurfaces," *Adv. Mater.* **33**(21), 2005864 (2021).
32. R. W. Gerchberg, "A practical algorithm for the determination of phase from image and diffraction plane pictures," *Optik* **35**, 237–246 (1972).
33. J. Burch and A. Di Falco, "Surface topology specific metasurface holograms," *Acs Photonics* **5**(5), 1762–1766 (2018).
34. G. Zheng, H. Mühlenbernd, M. Kenney, G. Li, T. Zentgraf, and S. Zhang, "Metasurface holograms reaching 80% efficiency," *Nat. Nanotechnol.* **10**(4), 308–312 (2015).
35. J. Burch, D. Wen, X. Chen, and A. Di Falco, "Conformable holographic metasurfaces," *Sci. Rep.* **7**(1), 4520 (2017).
36. L. Yan, J. Xiao, T. Plaskocinski, M. Biabanifard, S. Persheyev, M. Askari, and A. D. Falco, "Two-Tier Manipulation of Holographic Information (dataset)," University of St Andrews Research Portal (2022), <https://doi.org/10.17630/1907da8b-4e1f-4422-aa2c-3928218243fe>.